Bidirectional process prediction in the laser-induced-graphene production using blackbox deep learning

Maxim Polomoshnov[1*], Nitheesh M. Nair[1], Gerardo Hernandez-Sosa[1,2,3,4], Markus Reischl[1]

[1] Institute for Automation and Applied Informatics, Karlsruhe Institute of Technology, Hermann-von-Helmholtz-Platz 1, 76344 Eggenstein-Leopoldshafen, Germany

[2] Light Technology Institute, Karlsruhe Institute of Technology, Engesserstr. 13, 76131 Karlsruhe, Germany

[3] InnovationLab, Speyerer Str. 4, 69115 Heidelberg, Germany

[4] Institute of Microstructure Technology, Karlsruhe Institute of Technology, Hermann-von-Helmholtz-Platz 1, 76344 Eggenstein-Leopoldshafen, Germany

[*] Corresponding author. E-mail: maxim.polomoshnov@kit.edu

Supplementary Information

Supplementary Note S1. Blackbox Deep Learning

The engineering paradigm demands on a maximum transparency and the complete understanding of decision-making in any related process, to prove its reliability. Therefore, the input-to-output data transformation has to be fully interpretable and explainable[16,17,21]. A fully-parametric model forms a whitebox data transformer as a core of the analytical approach, indicated in Fig. S1. It requires an extended prior knowledge, including a deep analysis of related model features, of the decision-making transparency, and of the interim data visualization[10,18,19]. The knowledge also includes detailed submodels, the physics-informed approach, and digital-twin models to simulate physical rules of the real world. As a result, the model decision has to be completely explainable, and the output data completely reliable. In fact, design and tuning of a whitebox model is an intricate task, demanding on time and personnel qualification[18,19,25]. Hence, the approach is merely overcomplicated for the tasks that are possible to approximate with plain equations, such as interrelation of the applied energy, and dimensional, functional, and quality properties of laser-induced graphene (LIG) lines.

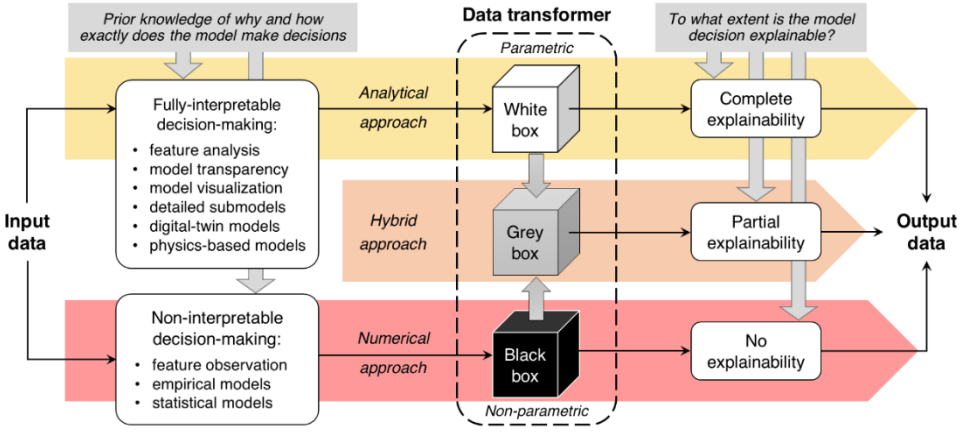

Supplementary Fig. S1. Schematic of the white, grey, and blackbox approaches to data transformation in decision-making models in machine-learning. Combined and adapted from [14,15,17–20].

With respect to deep learning (DL), a multilayer perceptron (MLP) forms a simple blackbox data transformer, interlinking input and output data directly, without any prior knowledge of the underlaying process[13–15,28]. Although it offers limited interpretability, the approach is adequate for plain LIG-fabrication tasks, where sophisticated physical modelling is impractical for economic reasons[22,25]. Thus, the employment of MLP to predict the input-output correlation in the LIG-based fabrication is expected to be a promising and powerful method.

Fabricated and assembled samples

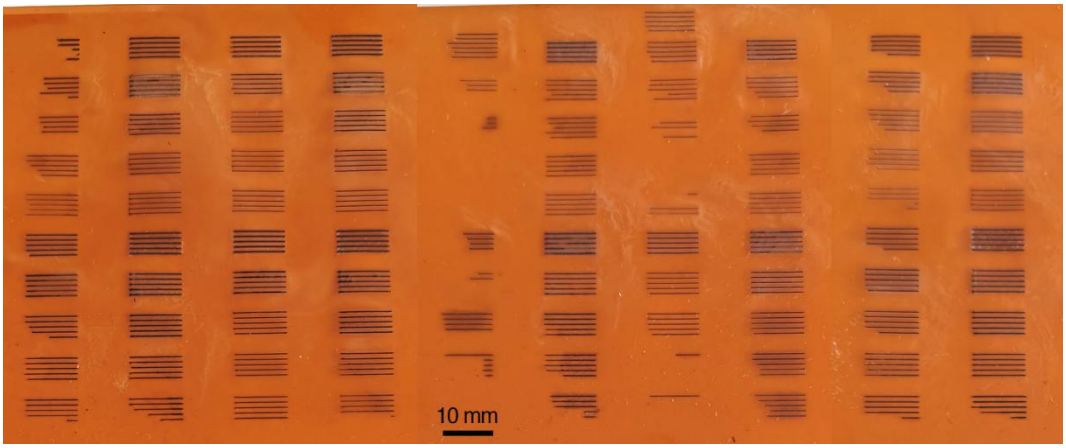

Supplementary Fig. S2. Combined digital photos of fabricated training lines, after detachment of the substrate (the scale is equal).

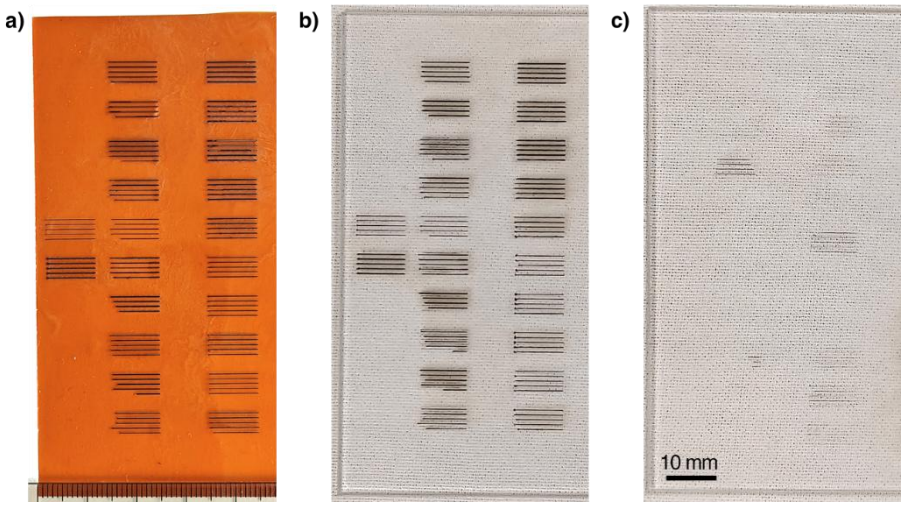

Supplementary Fig. S3. Digital photos of fabricated validation lines, after detachment of the substrate (the scale is equal). **a** Patterned substrate, **b** top glass slide, **c** bottom glass slide. Partly delaminated graphene transferred from the substrate and caused a significant variance in the measured line resistance is clearly visible in **b–c**.

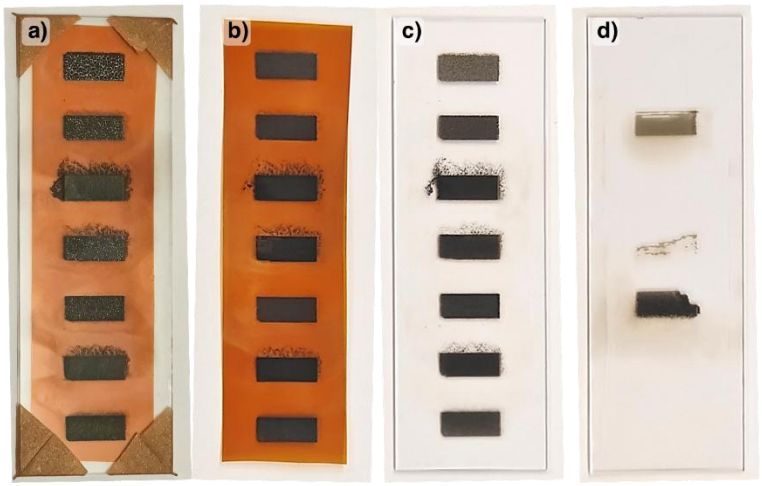

Supplementary Fig. S4. Digital photos of fabricated validation rectangles, using the direct-prediction workflow. **a** Substrate assembly, **b** patterned substrate, **c** top glass slide, **d** bottom glass slide. Partly delaminated graphene transferred from the substrate and corrupted two of the rectangles is clearly visible in **c–d**. Dimensions of the glass slides are 75 × 25 mm^2, with the same scale for all images.

Supplementary Table S1. Input and output laser-beam parameters and product properties, mutually applied and collected for fabrication and evaluation of validation samples.

Laser-beam parameters and product properties	**Value range**			
	Lines		**Rectangles**	
	Direct	**Inverse**	**Direct**	**Inverse**
Laser power P [W]	4.6–13.0	6.6–10.4	4.0–11.6	4.8–8.6
Laser movement speed across the substrate v [mm/s]	37–166	50.7–114.9	45–150	45–150
Laser-beam defocus D [mm]	-0.4–0.3	-0.1–0.1	-0.5–0.3	-0.4–0.3
Linear resistance R [Ω/mm], or (Resistance R_{eq} [Ω])	14.8–339.2	21.0–135.0	(11.0–81.5)	(10.9–87.8)
Line width W [µm]	184.8–267.4	124.0–286.0		
Line quality Q [1]	"0" or "1"	"0" or "1"	"0" or "1"	"0" or "1"

Note: The underlined values denote output data, the regular ones indicate input data.

Analysis of the training lines

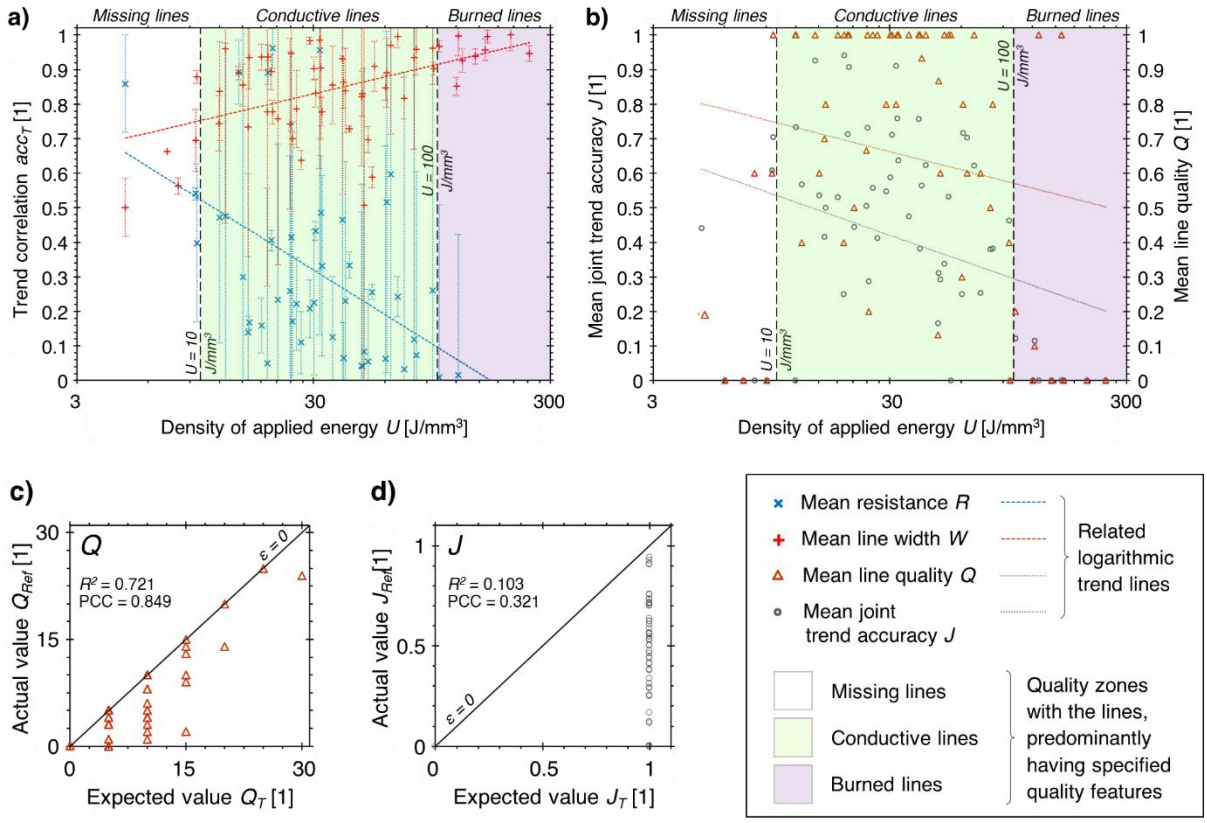

Supplementary Fig. S5. Analysis of the training lines (dataset A[32]). **a–b** Data distribution and identified quality zones, with respect to the applied density of laser energy U: **a** trend correlation for the linear resistance R and the line width W, and **b** data distribution for the line quality Q and the joint trend correlation J. For discrete Q and J, variance and error bars were omitted. Three zones were detected from the Q values: predominantly missing ($U \lessapprox 10$ J/mm³), conductive (10 J/mm³ $\lessapprox U \lessapprox 100$ J/mm³), and burned ($U \gtrapprox 100$ J/mm³) lines. **c–d** Individual correlation scatter plots for **c** Q and **d** J. Diagonal lines $\varepsilon = 0$ represent the complete match. In **c**, axes are graduated with the total number of samples related to the same U value. In **d**, the expected value was 0 or 1. Corresponding values of R^2 and of the Pearson correlation coefficient (PCC) are indicated.

Supplementary Table S2. Accuracy metrics for the training lines (dataset A[32]), in [1], n=500.

Metrics	***R***	***W***	***Q***	***J***
acc_T	0.313 ± 0.262	0.844 ± 0.125	0.767 ± 0.380	0.529 ± 0.289
Regression	0.329 ± 0.290	0.666 ± 0.296	0.001 ± 0.001	0.454 ± 0.324
R^2	0.192	0.490	0.721	0.103
PCC	0.438	0.700	0.849	0.321

Analysis of the validation lines

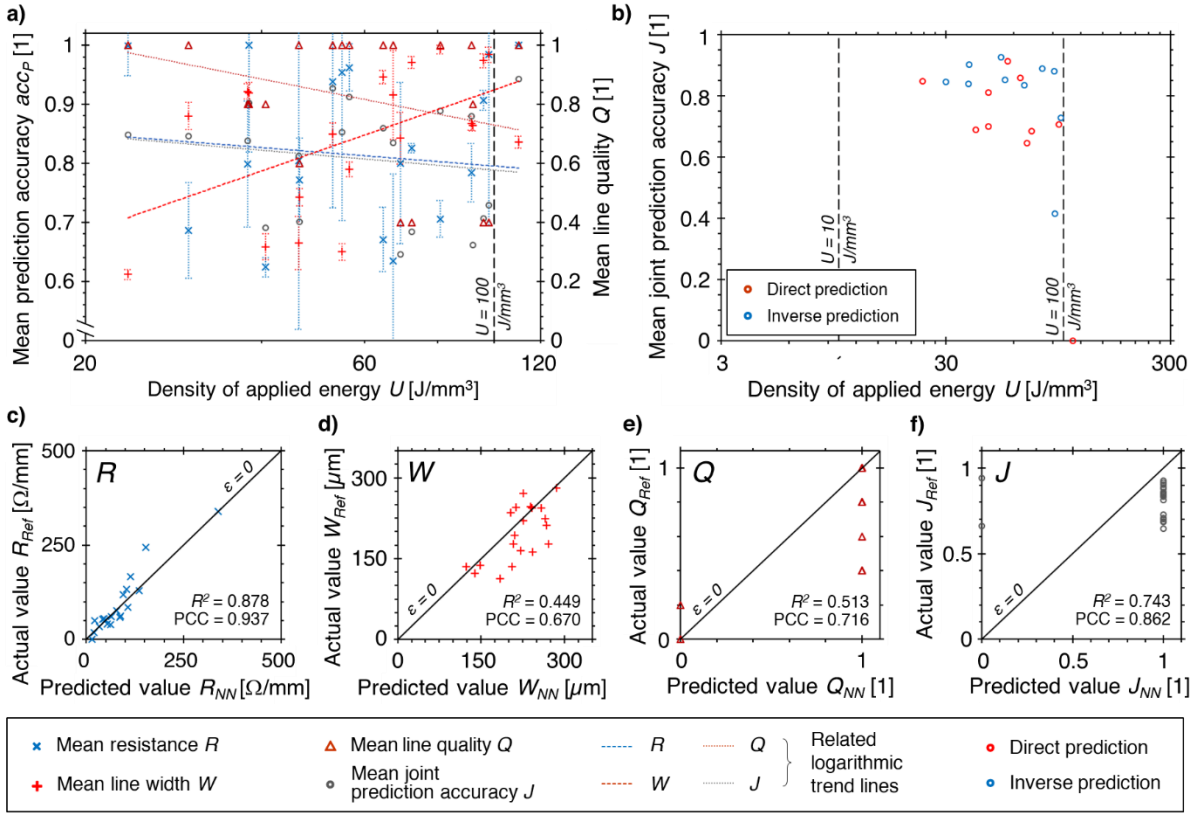

Supplementary Fig. S6. Analysis of the validation lines (dataset B[32]). **a** Mean prediction accuracy for the linear resistance *R*, the line width *W*, the line quality *Q*, and the joint accuracy *J*, with respect to the applied density of laser energy *U*. **b** Mean joint prediction accuracy *J*, with respect to *U* and to direction of the prediction workflow. **c–f** Individual correlation scatter plots for **c** *R*, **d** *W*, **e** *Q*, and **f** *J*. Diagonal lines $\varepsilon = 0$ represent the complete match. Corresponding values of R^2 and of the Pearson correlation coefficient (PCC) are indicated.

Supplementary Table S3. Accuracy metrics for the validation lines (dataset B[32]), in [1], n=100.

Metrics	***R***	***W***	***Q***	***J***
acc_P	0.813 ± 0.154	0.844 ± 0.117	0.820 ± 0.236	0.808 ± 0.094
Regression	0.592 ± 0.315	0.784 ± 0.176	0.795 ± 0.388	0.627 ± 0.319
R^2	0.878	0.449	0.513	0.743
PCC	0.937	0.670	0.716	0.862

Analysis of the validation rectangles

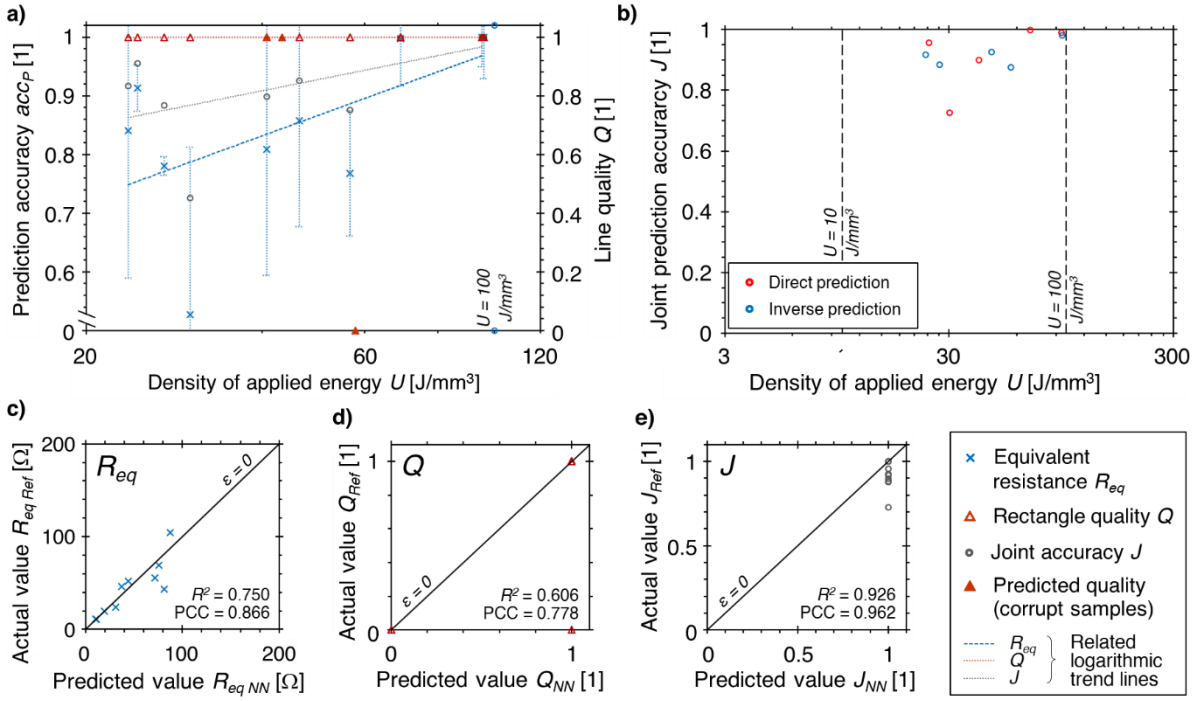

Supplementary Fig. S7. Analysis of the validation rectangles (dataset C[32]). **a** Prediction accuracy for the equivalent resistance R_{eq}, the rectangle quality Q, and the joint accuracy J, with respect to the applied density of laser energy U. **b** Mean joint prediction accuracy J, with respect to U and to direction of the prediction workflow. **c–e** Individual correlation scatter plots for **c** R_{eq}, **d** Q, and **e** J. Diagonal lines $\varepsilon = 0$ represent the complete match. Corresponding values of R^2 and of the Pearson correlation coefficient (PCC) are indicated.

Supplementary Table S4. Accuracy metrics for the validation rectangles (dataset C[32]), in [1], n=10.

Metrics	R_{eq}	Q	J
acc_P	0.849 ± 0.137	0.923 ± 0.266	0.918 ± 0.078
Regression	0.749 ± 0.137	0.538 ± 0.458	0.585 ± 0.149
R^2	0.750	0.606	0.926
PCC	0.866	0.778	0.962

Analysis of the twofold control

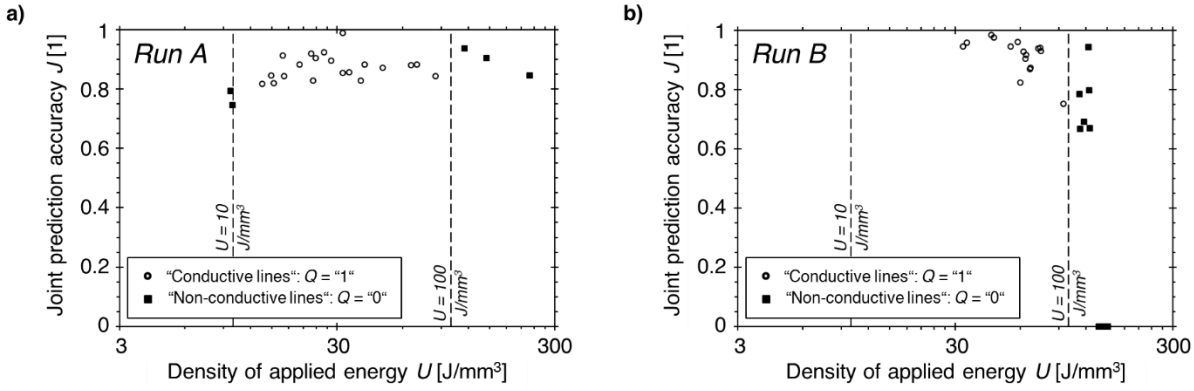

Supplementary Fig. S8. Analysis of the twofold control (dataset D[32]). Mean joint prediction accuracy J, with respect to U and to related quality zones: **a** in the run A (restoration of the laser-beam parameters), and **b** in the run B (restoration of the product properties).

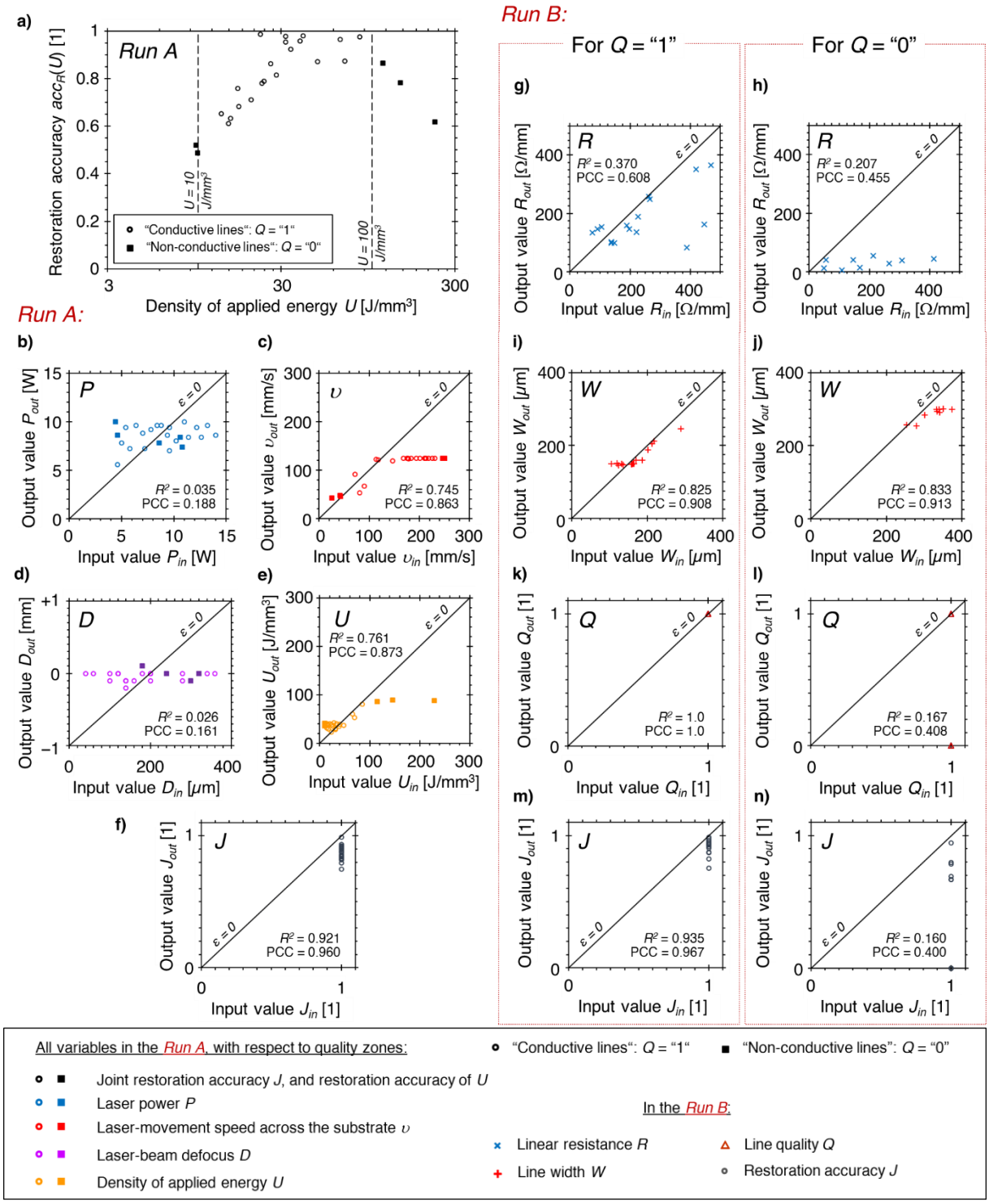

Supplementary Fig. S9. Analysis of the twofold control (dataset D[32]). **a** Restoration accuracy of the applied density of laser energy U, with respect to its value, in the run A. **b–n** Individual correlation scatter plots for **b** laser power P, **c** movement speed across the substrate υ, **d** laser-beam defocus D, **e** U, **f** joint restoration accuracy J in the run A, **g–h** linear resistance R, **i–j** line width W, **k–l** line quality Q, **m–n** joint restoration accuracy J in the run B. The plots in **g**, **i**, **k**, and **m** indicate results for the quality zone "conductive lines", in **h**, **j**, **l**, and **n** for "non-conductive lines", such as missing and burned ones. Diagonal lines $\varepsilon = 0$ represent the complete match. The plots in **b–f** are related to the run A (restoration of the laser-beam parameters), in **g–n** to the run B (restoration of the product properties). Corresponding values of R^2 and of the Pearson correlation coefficient (PCC) are indicated.

Supplementary Table S5. Accuracy metrics for the twofold control (dataset E, run A[32]), depending on the quality zone, in [1].

Quality zone	Metrics	***P***	***υ***	***D***	***J***	***U***
All lines, n = 25	acc_P	0.765 ± 0.138	0.681 ± 0.137	0.848 ± 0.092	0.868 ± 0.050	0.802 ± 0.149
	Regression	0.856 ± 0.081	0.426 ± 0.195	0.822 ± 0.109	0.669 ± 0.249	0.068 ± 0.557
	R^2	0.035	0.745	0.026	0.921	0.761
	PCC	0.188	0.863	0.161	0.960	0.873
Conductive lines, n = 20	acc_P	0.789 ± 0.118	0.681 ± 0.121	0.850 ± 0.098	0.874 ± 0.041	0.838 ± 0.126
	Regression	0.872 ± 0.111	0.460 ± 0.158	0.764 ± 0.147	0.748 ± 0.286	0.528 ± 0.301
	R^2	0.142	0.549	0.041	0.955	0.658
	PCC	0.376	0.741	0.201	0.977	0.811
Missing and burned lines, n = 5	acc_P	0.672 ± 0.169	0.680 ± 0.187	0.842 ± 0.063	0.845 ± 0.070	0.655 ± 0.147
	Regression	0.845 ± 0.070	0.243 ± 0.376	0.616 ± 0.210	0.620 ± 0.197	0.322 ± 0.301
	R^2	0.589	0.999	0.484	0.961	0.803
	PCC	-0.767	0.999	-0.696	0.980	0.896

Supplementary Table S6. Accuracy metrics for the twofold control (dataset E, run B[32]), depending on the quality zone, in [1].

Quality zone	Metrics	***R***	***W***	***Q***	***J***
All lines, n = 25	acc_P	0.523 ± 0.301	0.887 ± 0.064	0.880 ± 0.325	0.768 ± 0.299
	Regression	0.432 ± 0.284	0.811 ± 0.101	0.880 ± 0.325	0.745 ± 0.290
	R^2	0.238	0.953	0.220	0.203
	PCC	0.488	0.976	0.469	0.450
Conductive lines, n = 16	acc_P	0.696 ± 0.191	0.885 ± 0.070	1.0 ± 0.0	0.915 ± 0.056
	Regression	0.641 ± 0.210	0.813 ± 0.120	1.0 ± 0.0	0.821 ± 0.105
	R^2	0.370	0.825	1.0	0.935
	PCC	0.608	0.908	1.0	0.967
Missing and burned lines, n = 9	acc_P	0.214 ± 0.193	0.891 ± 0.051	0.667 ± 0.471	0.506 ± 0.367
	Regression	0.051 ± 0.039	0.752 ± 0.100	0.667 ± 0.471	0.472 ± 0.342
	R^2	0.207	0.833	0.167	0.160
	PCC	0.455	0.913	0.408	0.400

Supplementary Note S2. Demonstrator

The full resistance of each LIG electrode R_{LIG} was defined as in Equation S1. Then, the required linear resistance R^*_{LIG} and line width W^*_{LIG} were found as in Equations S2 and S3, respectively.

$$R_{LIG} = \frac{1}{2} \cdot \frac{V_{DD} - V_{LED}}{I_{LED}}, \quad [\Omega], \tag{S1}$$

with V_{DD} = 5 V — power-source voltage,
V_{LED} = 1.8 V, I_{LED} = 2 mA — LED voltage and current, correspondingly.

$$R^*_{LIG} = \frac{R_{LIG}}{l_{LIG}}, \quad [\Omega/mm], \tag{S2}$$

with l_{LIG} = 20 mm — single-electrode length, chosen for functional reasons.

$$W^*_{LIG} = \frac{l_{LIG}}{\sigma_{LIG} \cdot R_{LIG} \cdot t_{PI} \cdot \alpha} \cdot 10^6, \quad [\mu m], \tag{S3}$$

with σ_{LIG} = 15 S/cm — approximated LIG conductivity[35–37],
t_{PI} = 75 µm — substrate thickness,
α = 0.9 — non-squareness correction factor for the cross-section area.

Supplementary Note S3. Comparison to literature

In Table S7, outcomes of the present work are compared to the related results reported in literature. For each work, *application field*, *employed model*, and *dataset size* are pointed out. The *ML subset* specifies belonging of the model to the ML or DL field, and indicates its vision-based focus, where appropriate. The *plain workflow* indicates whether a simplistic approach was utilized, or the model employed any complex workflow, such as using of physics-informed data, multiple-model frameworks, Bayesian optimization of hyperparameters; or required an extensive prior knowledge on the underlaying process, or sophisticated analytical equipment. *Prefiltered data* labels conducted sample preselection to process merely high-quality data, aimed to increase reported prediction accuracy. Noted *classification task* means a simplified result-qualification objective, which is usually less demanding, and ensures a higher prediction accuracy than regression analysis (i.e., result-quantification objective). Among multiple *reported mean accuracies*, the highest one was chosen and listed in Table S7 for each work, according to the employed model. For significantly distinct outcomes of one work, all corresponding results were outlined.

Supplementary Table S7. Comparison to literature.

Reference	Application field	Employed model	ML subset	Plain workflow	Dataset size [samples]	Prefiltered data	Classification task	Reported mean accuracy, or indicated metrics
Present work	LIG	Blackbox MLP model, double-direction	DL	Yes	500	No	No	80.8 % – 94.8 % R^2 = 0.74–0.96 PCC = 0.86–0.98
[9]	Fluoride-doped LIG	Bayesian-optimized Gaussian Process Regression model	ML	No	201	Yes	No	89.7 %
[11]	LIG	Random Forest and XGB framework	ML	No	570	Yes	No	91.25 %
[12]	LIG	Digital-twin, single-layer MLP model	ML	No	648	Yes	Yes Yes No	96.9 % (resistance) 88.9 % (morphology) R^2 = 0.91
[22]	LIG	Twofold transfer learning model	DL, vision-based	No	500	No	Yes	95.4 %
[23]	Flash graphene	Digital-twin, physics-informed multi-NN framework	ML	No	173	Yes	No	R^2 = 0.81
[24]	LIG	K-Nearest Neighbors model	ML	Yes	103	Yes	No	94.3 %
[26]	Flash graphene	XGB model	ML	Yes	> 20,000	No	No	R^2 = 0.80
[27]	Nickel-graphene nanocomposites	Long short-term memory model	DL	No	48,600	No	No	PCC = 0.95
[28]	Inkjet printing	Twofold physics-informed MLP model	DL	No	883,000	No	Yes	R^2 = 0.98
[29]	Inkjet printing	Physics-informed framework	DL, vision-based	No	10,800	No	Yes, partly	Similarity index = 0.862
[30]	Additive manufacturing: laser powder bed fusion	Physics-informed MLP model, double-direction	DL	No	103	Yes	No	59.0 % (on pure physically-manufactured data) 96.6 % (on hybrid physics-informed data)